

TIDAL STELLAR DISRUPTIONS BY MASSIVE BLACK HOLE PAIRS. II. DECAYING BINARIES

XIAN CHEN^{1,2,5}, ALBERTO SESANA^{3,4}, PIERO MADAU², AND F. K. LIU^{1,5}

¹ Department of Astronomy, Peking University, 100871 Beijing, China; fkliu@pku.edu.cn

² Department of Astronomy & Astrophysics, University of California, 1156 High Street, Santa Cruz, CA 95064, USA

³ Kavli Institute for Astronomy and Astrophysics, Peking University, 100871 Beijing, China

⁴ Center for Gravitational Wave Physics, The Pennsylvania State University, University Park, State College, PA 16802, USA

⁵ Max-Planck-Institut für Gravitationsphysik (Albert Einstein Institute), Am Mühlenberg, 14476 Golm, Germany

Received 2010 May 9; accepted 2010 December 22; published 2011 February 4

ABSTRACT

Tidal stellar disruptions have traditionally been discussed as a probe of the single, massive black holes (MBHs) that are dormant in the nuclei of galaxies. We have previously used numerical scattering experiments to show that three-body interactions between bound stars in a stellar cusp and a non-evolving “hard” MBH binary will also produce a burst of tidal disruptions, caused by a combination of the secular “Kozai effect” and by close resonant encounters with the secondary hole. Here, we derive basic analytical scalings of the stellar disruption rates with the system parameters, assess the relative importance of the Kozai and resonant encounter mechanisms as a function of time, discuss the impact of general relativistic (GR) and extended stellar cusp effects, and develop a hybrid model to self-consistently follow the shrinking of an MBH binary in a stellar background, including slingshot ejections and tidal disruptions. In the case of a fiducial binary with primary hole mass $M_1 = 10^7 M_\odot$ and mass ratio $q = M_2/M_1 = 1/81$, embedded in an isothermal cusp, we derive a stellar disruption rate $\dot{N}_* \sim 0.2 \text{ yr}^{-1}$ lasting $\sim 3 \times 10^5 \text{ yr}$. This rate is three orders of magnitude larger than the corresponding value for a single MBH fed by two-body relaxation, confirming our previous findings. For $q \ll 0.01$, the Kozai/chaotic effect could be quenched due to GR/cusp effects by an order of magnitude, but even in this case the stellar-disruption rate is still two orders of magnitude larger than that given by standard relaxation processes around a single MBH. Our results suggest that $\gtrsim 10\%$ of the tidal-disruption events may originate in MBH binaries.

Key words: black hole physics – galaxies: active – galaxies: kinematics and dynamics – galaxies: nuclei – gravitational waves – methods: numerical

Online-only material: color figures

1. INTRODUCTION

Stars that wander too close to the massive black holes (MBHs) that reside at the centers of galaxies are shredded by the tidal gravitational field of the hole. After a tidal disruption event, about half of the debris is spewed into eccentric bound orbits and falls back onto the hole, giving rise to a bright UV/X-ray outburst that may last for a few years (e.g., Rees 1988). “Tidal flares” from MBHs may have been observed in several nearby inactive galaxies (Komossa 2002; Esquej et al. 2007). The inferred stellar disruption frequency is $\sim 10^{-5} \text{ yr}^{-1}$ per galaxy (with an order of magnitude uncertainty; Donley et al. 2002), comparable to the theoretical expectations for single MBHs fed by two-body relaxation (Wang & Merritt 2004).

Yet MBHs are not expected to grow in isolation. According to the standard paradigm of structure formation in the universe, galaxies merge frequently during the assembly of their dark matter halos. As MBHs become incorporated into larger and larger halos, they sink to the center of the more massive progenitor owing to dynamical friction from distant stars and form bound massive black hole binaries (MBHBs). In a purely stellar background, as the binary separation decays, the effectiveness of dynamical friction slowly declines, and the pair then “hardens” via three-body interactions, i.e., by capturing stars that pass close to the holes and ejecting them at much higher velocities (e.g., Begelman et al. 1980; Quinlan 1996; Volonteri et al. 2003; Sesana et al. 2006). If the hardening continues sufficiently far, possibly driven by efficient stellar relaxation processes in a triaxial potential (e.g., Merritt & Poon 2004) or in the presence of massive perturbers (e.g., Perets et al. 2007;

Perets & Alexander 2008), or by dissipative gaseous processes (e.g., Colpi & Dotti 2009), gravitational radiation losses finally take over, and the two MBHs will coalesce in less than a Hubble time (e.g., Merritt & Milosavljević 2005; Sesana et al. 2005, 2007). In Chen et al. (2009), we used scattering experiments to show that gravitational slingshot interactions between a non-evolving, unequal-mass hard binary and a bound stellar cusp will inevitably be accompanied by a burst of stellar tidal disruptions. Our results differed from those of Ivanov et al. (2005), who developed an analytical theory of the secular evolution of stellar orbits in the gravitational field of an MBHB, and of Chen et al. (2008), who argued that stellar disruption rates by MBHBs fed by two-body relaxation would be smaller than those expected for single MBHs. Our numerical experiments revealed that a significant fraction of stars initially bound to the primary hole are scattered into its tidal disruption loss cone by resonant interactions with the secondary hole, close encounters that change the stellar orbital parameters in a chaotic way.

In this paper, we continue our investigations of stellar disruptions by MBHBs embedded in bound stellar cusps. We develop a hybrid model that self-consistently follows over time the shrinking of an MBHB, the evolution of the stellar cusp, and the stellar disruption rate. The plan is as follows. In Section 2, we introduce the basic theory of stellar disruption processes by MBHB systems. We describe our numerical scattering experiments in Section 3, and discuss our results for different binary parameters as well as the effect of general relativistic (GR) corrections in Section 4. A detailed study of the properties of disrupted stars is carried out in Section 5. As a first step toward understanding the dependence of stellar consumption on the parameters of

the system, in Section 6 we fix the binary semimajor axis and its eccentricity, and calculate the stellar disruption rate in the stationary case. In Section 7, we present our hybrid model and calculate the disruption rates for an evolving, shrinking MBHB. Finally, we summarize and discuss our results in Section 8.

2. BASIC THEORY OF STELLAR DISRUPTIONS

Consider an isotropic background of stars all of mass m_* and radius r_* centered on an MBH. Let $\Psi(r)$ be the total gravitational potential at radius r and $r_t = r_*(M_{\text{BH}}/m_*)^{1/3}$ the tidal disruption radius:

$$r_t \simeq 5 \times 10^{-6} \text{pc} \left(\frac{r_*}{R_\odot} \right) \left(\frac{M_\odot}{m_*} \right)^{1/3} \left(\frac{M_{\text{BH}}}{10^7 M_\odot} \right)^{1/3}. \quad (1)$$

The phase-space region of specific energy E_* and specific angular momentum J_* bounded by

$$J_{\text{lc}}^2(E_*, r_t) = 2r_t^2[E_* - \Psi(r_t)] \quad (2)$$

is populated by stars on orbits crossing r_t and thus susceptible to tidal disruption. We name this cone-like region of phase space the ‘‘tidal loss cone.’’ Whether the tidal loss cone can be emptied by stellar disruption depends on the efficiency of stellar relaxation. Let $T_r(E_*)$ be the relaxation timescale of stars with specific energy E_* , $P_*(E_*)$ their orbital period, and $J_c(E_*)$ the specific angular momentum of a circular orbit with energy E_* . In the ‘‘pinhole limit’’ (Lightman & Shapiro 1977), $P_*(E_*)/T_r(E_*) \gg J_{\text{lc}}^2(E_*, r_t)/J_c^2(E_*)$, a star can random walk in and out of the tidal loss cone within one orbital period, and the tidal loss cone remains almost full despite tidal disruptions. In the ‘‘diffusion limit,’’ $P_*(E_*)/T_r(E_*) \lesssim J_{\text{lc}}^2(E_*, r_t)/J_c^2(E_*)$, the tidal loss cone is emptied after a single orbital period, and stars diffuse into the loss cone on the relaxation timescale. Assume now that the central primary hole of mass M_1 forms a binary pair with a secondary hole of mass $M_2 < M_1$, and let a be the semimajor axis of the system. The $E_* - J_*$ region of phase space bounded by

$$J_{\text{lc}}^2(E_*, a) = 2a^2[E_* - \Psi(a)] \quad (3)$$

is composed of orbits that are either inside or intersect a sphere of radius a . If the binary is ‘‘hard,’’ a star on such an orbit will undergo a three-body interaction with the MBHB, so we refer to the phase space defined by Equation (3) as the ‘‘interaction loss cone.’’ Three-body interactions perturb the energy and angular momentum of ‘‘intruder’’ stars, acting as an additional source of stellar relaxation. If three-body relaxation occurs in the diffusion regime, the stellar consumption rate will be enhanced.

To proceed further, we must first define some characteristic scales of an MBHB system. Recent numerical simulations have shown that three-body interactions between the binary and intruder stars result in significant energy exchange when the total stellar mass within the binary orbit is comparable to or smaller than the mass of the secondary hole (Baumgardt et al. 2006; Matsubayashi et al. 2007). We denote by a_0 such a critical binary separation: the binary shrinks by dynamical friction when $a \gtrsim a_0$, and by three-body processes at smaller separations. Following Sesana et al. (2008), we assume that the stellar distribution follows a double power law with break radius r_0 , defined as the radius of the ‘‘sphere of influence’’ containing a mass in stars equal to $2M_1$. For $r > r_0$, the stellar density profile follows an isothermal distribution,

$$\rho_*(r) = \frac{\sigma_*^2}{2\pi G r^2}, \quad (4)$$

where σ_* is the one-dimensional velocity dispersion, while for $r < r_0$ $\rho_*(r) \propto r^{-\gamma}$. It is then easy to derive

$$r_0 = (3 - \gamma)GM_1/\sigma_*^2 \simeq 4.6 \text{pc}(3 - \gamma)M_7\sigma_{100}^{-2} \quad (5)$$

and $a_0 = q^{1/(3-\gamma)}r_0$, where $M_7 \equiv M_1/10^7 M_\odot$, $q \equiv M_2/M_1$ is the binary mass ratio and $\sigma_{100} \equiv \sigma_*/100 \text{km s}^{-1}$. Note that the ‘‘three-body radius’’ a_0 is larger than the conventional ‘‘hardening’’ radius $a_h = GM_2/(4\sigma_*^2)$ (Quinlan 1996). The ratio between the tidal radius of the primary hole, r_{t1} , and a_0 ,

$$\frac{r_{t1}}{a_0} \simeq \frac{10^{-6}}{3 - \gamma} q^{-p} \frac{\sigma_{100}^2}{M_7^{2/3}} \left(\frac{r_*}{R_\odot} \right) \left(\frac{M_\odot}{m_*} \right)^{1/3}, \quad (6)$$

where $p \equiv 1/(3 - \gamma)$, indicates that the interaction loss cone of a binary is much larger than the tidal loss cone of a single MBH. Therefore, the transfer of only a small fraction of interacting stars into the tidal loss cone will cause a large enhancement of the stellar disruption rate.

When does the presence of a binary begin affecting the stellar disruption rate? Let us assume that, before the intrusion of the secondary hole, stellar relaxation is dominated by two-body interactions. Stars in the diffusion limit are bound to the primary hole, and their specific energy E_* is related to the orbital semimajor axis a_* by $E_* = -GM_1/(2a_*)$. The boundary between the pinhole and diffusion limits is then dictated by the condition

$$P_*(a_*)/T_r(a_*) = J_{\text{lc}}^2(a_*, r_{t1})/J_c^2(a_*) = r_{t1}/a_*. \quad (7)$$

Substituting into the above equation the two-body relaxation timescale

$$\begin{aligned} T_r(r) &= \frac{\sqrt{2}\sigma_*^3}{\pi G^2 m_* \rho_*(r) \ln \Lambda} \\ &= 5 \text{Gyr} \sigma_{100} \left(\frac{10}{\ln \Lambda} \right) \left(\frac{r_0}{1 \text{pc}} \right)^2 \left(\frac{r}{r_0} \right)^\gamma \end{aligned} \quad (8)$$

(where $\ln \Lambda$ is the Coulomb logarithm) and the Keplerian orbital period of the star orbiting M_1 , $P_*(a_*) = 2\pi[a_*^3/(GM_1)]^{1/2}$, and assuming $r_* = R_\odot$ and $m_* = M_\odot$, we can write the critical radius a_c marking the boundary between pinhole and diffusion regimes as

$$\frac{a_c}{r_0} \simeq 0.33^{2/s} (3 - \gamma)^{-1/s} M_7^{2/3s} \sigma_{100}^{4/s} \left(\frac{\ln \Lambda}{10} \right)^{-2/s}, \quad (9)$$

where $s \equiv 5 - 2\gamma$. If a secondary hole is now added to the system, and the interaction loss cone is not empty, a significant enhancement of stellar disruptions occurs when the binary separation shrinks to $a \sim a_c$. For an isothermal density profile and a primary hole satisfying the $M_{\text{BH}} - \sigma_*$ relation, $M_7 = \sigma_{100}^4$ (Tremaine et al. 2002), Equation (9) implies $a_c > a_0$ as long as $q < 0.1 M_7^{5/3}$, i.e., for unequal-mass binaries the enhancement of stellar disruptions starts during the dynamical friction early phases of the binary orbital evolution. N -body simulations have shown, however, that the secondary hole decays from a_c to a_0 and enters the three-body interaction regime on a timescale $< 10^5$ yr. Here, we ignore the early dynamical friction phases and focus on stellar disruptions induced by three-body scattering events. At binary separation $a = a_0$, the interaction loss cone contains stars that can be bound or unbound to the primary. A

bound star can interact with the binary multiple times before leaving the system, significantly increasing its probability of being tidally disrupted. For equal-mass binaries, the radius of influence r_0 is comparable to the three-body radius a_0 , and most scattering events involve stars that are unbound (or marginally bound). The impact of bound stars is more important for unequal-mass MBHBs, and these systems will be the main focus of this paper.

A bound star with semimajor axis $a_* < a/2$ never crosses the orbit of the secondary hole and undergoes a secular evolution in which its orbital eccentricity is excited and oscillates periodically, the so-called Kozai effect (Kozai 1962; Lidov 1962; Ivanov et al. 2005; Gualandris & Merrit 2009). The period of oscillation (“Kozai timescale”) is

$$T_K(a_*) = \frac{2}{3\pi q} \left(\frac{a_*}{a}\right)^{-3/2} P(a) \quad (10)$$

(Innanen et al. 1997; Kiseleva et al. 1998), where

$$P(a) = 2\pi a^{3/2} [G(M_1 + M_2)]^{-1/2} \\ \simeq 10^3 \text{ yr} (1+q)^{-1/2} M_7^{-1/2} \left(\frac{a}{0.1 \text{ pc}}\right)^{3/2} \quad (11)$$

is the orbital period of the binary. Since $T_K(a) \ll T_r(a)$, the Kozai mechanism is much more efficient than two-body interactions at repopulating the tidal loss cone. However, when $q \ll 1$, $r_0 \gg a_0$ and the majority of bound stars have close encounters with the secondary hole that change the orbital elements of the star in a complicated chaotic way. In this regime, (1) numerical simulations are needed to give reasonable estimates of the tidal disruption rates and (2) the contribution to the gravitational potential by background stars as well as stellar collisions can be neglected during the interaction. When $a_* \ll a$, two-body relaxation can be more efficient than Kozai precession in changing stellar orbits (compare Equations (8) and (10), and note that $\sigma_*^2 \propto a_*^{-1}$ at $a_* \ll r_0$), but the number of these stars is negligible. Under these conditions, the problem can be tackled by means of restricted three-body scattering experiments.

3. SCATTERING EXPERIMENTS

The integration of the three-body encounter equations is performed in a coordinate system centered at the location of M_1 . Initially, the binary (of mass ratio q and eccentricity e) has a randomly oriented orbit with M_2 at its pericenter: stars move in the x - y plane with pericenters along the positive x -axis and random orbital phases. The initial conditions of the restricted three-body problem are then completely defined by six variables, three for the binary and three for the star:

1. the inclination of the orbit of the binary, θ , i.e., the angle between the angular momentum of the binary and the z -axis;
2. the longitude of the secondary hole ascending node, l ;
3. the argument of the pericenter of the secondary hole, ϕ (if $e \neq 0$);
4. the semimajor axis of the stellar orbit, a_* ;
5. the normalized (by the angular momentum of a circular orbit with the same semimajor axis) angular momentum of the star, j_* ; and
6. the orbital phase of the star, p_* .

We start each scattering experiment by generating six random numbers, with $\cos \theta$ evenly sampled in the range $[-1, 1]$, and

both l and ϕ uniformly distributed in the range $[0, 2\pi]$. We sample a_* logarithmically around a (the range is described in detail below) and j_*^2 randomly between 0 and 1 (corresponding to an isotropic distribution). Given the j_* of a star, we numerically integrate one revolution of a Keplerian orbit with eccentricity $e_* = (1 - j_*^2)^{1/2}$ and derive $p_*(t)$ as a function of time t . Then the initial orbital phase for the scattering experiment is drawn from the distribution function $f(p_*) = dt/dp_*$.

Having defined the initial conditions, the orbit of each star was followed by integrating the coupled first-order differential equations

$$\dot{\mathbf{r}} = \mathbf{v} \quad (12)$$

$$\dot{\mathbf{v}} = -G \sum_{i=1}^2 \frac{M_i(\mathbf{r} - \mathbf{r}_i)}{|\mathbf{r} - \mathbf{r}_i|^3}, \quad (13)$$

where \mathbf{r} and \mathbf{v} are the position and velocity vectors of the star and \mathbf{r}_i is the position of the i th ($i = 1, 2$) MBH. When $e \neq 0$, we included a subroutine to numerically compute the positions of the two holes at each time step. The units in the numerical computation were $G = M_{12} = a = 1$ (with $M_{12} \equiv M_1 + M_2$) and the integrator was an explicit Runge–Kutta method of order eight (**dopri8**; Hairer et al. 1987), with a fractional error per step in position and velocity set to 10^{-13} . The integration was stopped if one of the following conditions was satisfied: (1) the star left the sphere of radius $a(10^{10}q)^{1/4}$, where the quadrupole force from the binary is 10 orders of magnitude smaller than GM_{12}/a^2 , with positive energy; (2) the physical integration timescale exceeded 10^{10} yr; (3) the number of required integration time steps reached 10^8 . Conditions (2) and (3) were adopted to save computational time, as a small fraction ($\lesssim 3\%$ depending on q and e) of stars are scattered into wide, bound orbits and may survive many revolutions. We have tested our code by reproducing Figures 4 and 6 of Sesana et al. (2008) (who used full three-body scattering experiments) and found excellent agreement.

4. TESTS

To understand the dependence of our results on various properties of the MBHB, such as q and e , and the impact of GR effects, we performed a number of tests with $N = 10^4$ stars in each run. The initial semimajor axis of the intruder star was sampled logarithmically in the interval $[1/2a, 2a]$, where three-body interactions are expected to be the strongest. We recorded the minimum separation between the stars and the holes during each scattering experiment and analyzed the results in terms of the fraction of stars reaching a given distance from a member of the pair. In the case of unbound stars, if the initial distribution of pericenter distances is uniform, this fraction has the physical meaning of a close-encounter cross section (Chen et al. 2008). While for the bound stars considered here, the concept of cross section no longer strictly applies because the initial pericenter-distance distribution is not uniform, for convenience we shall still refer to this fraction as the close-encounter cross section in the following.

4.1. Close-encounter Cross Section

We performed scattering experiments for $q = 1/81$ and $e = 0.1$, where each star was allowed to encounter the binary as many times as required before the integration was stopped.

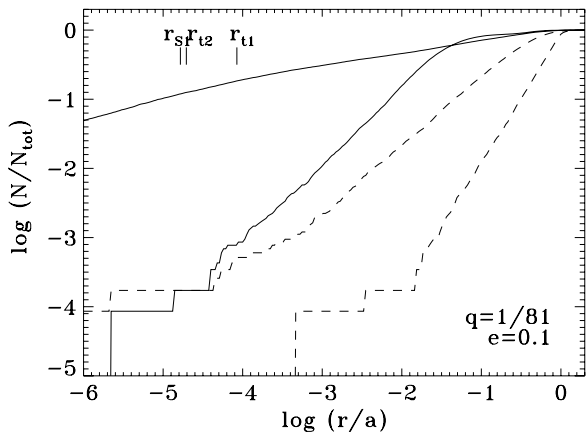


Figure 1. Close-encounter probability for bound stars interacting with an MBHB of mass ratio $q = 1/81$ and orbital eccentricity $e = 0.1$. The vertical axis shows the fraction of stars N/N_{tot} with closest approach distance $r_{\text{min}} < r$. Solid lines: multi-encounter cross section. Dashed lines: single encounter cross section. The upper solid and dashed curves refer to the primary hole, the lower ones to the secondary. The short vertical lines mark the positions of the tidal and Schwarzschild radii of the two holes for $M_7 = 1$, $\sigma_{100} = 1$, $a = a_0$, and $\gamma = 2$. The sharp cutoff at $N/N_{\text{tot}} \approx 10^{-4}$ is an artifact of small number statistics in the scattering experiments.

Then the minimum separation between the star and each hole during the entire course of the interaction was recorded for the calculation of the “multi-encounter cross section.” We also recorded the first minimum separation (a local minimum in the distance–time curve) during the encounter between the star and each hole, and calculated the “single-encounter cross section.” The latter can be viewed as the interaction probability in the case of an isolated MBH. The resulting cross sections are plotted in Figure 1. As already shown by Chen et al. (2009), the multi-encounter cross section for M_1 is dramatically higher than the single-encounter probability: when $r \approx 10^{-4}a$, corresponding to the tidal radius of a primary hole with $M_7 = 1$ embedded in an isothermal cusp with $\sigma_{100} = 1$, at separation $a = a_0$, the multi-encounter cross section of M_1 is nearly 3 dex larger than that for single encounters. In the following, we shall refer to the multi-encounter cross section at r_{t1} as the “tidal disruption cross section.” Because this is much larger than the corresponding cross section for the secondary, stellar disruptions by an unequal-mass binary will be dominated by the primary hole, and will be the focus of our analysis.

4.2. Dependence on q and e

To study the dependence of the close-encounter cross section on the binary mass ratio, we performed three additional sets of scattering experiments for $e = 0.1$ and $q = 1/9$, $1/243$, and $1/729$, each using 10^4 stars. The results show (Figure 2) that, as q increases, the multi-encounter probability decreases from 41% ($q = 1/729$) to 1.1% ($q = 1/9$). This is because, as the perturbing force from the secondary hole becomes stronger, a star is more susceptible to ejection. Figure 3 shows the dependence of the multi-encounter cross section on binary eccentricity at fixed $q = 1/81$. For $r/a > 10^{-6}$, the cross section varies at most by a factor of three as e increases from 0.1 to 0.9. When $r_{t1}/a \approx 10^{-4}$, the tidal disruption probability does not depend significantly on eccentricity.

5. PROPERTIES OF DISRUPTED STARS

To understand the physical processes responsible for the enhancement of the tidal disruption probability, we need to in-

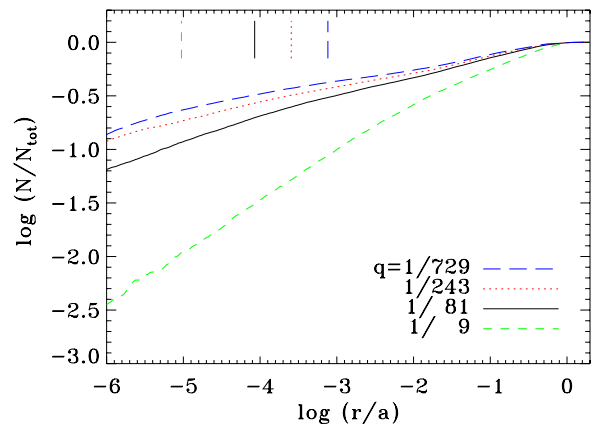


Figure 2. Multi-encounter cross section for bound stars interacting with the primary hole of an MBHB with $e = 0.1$ and different mass ratios q . The short vertical lines mark the locations of the tidal radii of M_1 for the same parameters used in Figure 1.

(A color version of this figure is available in the online journal.)

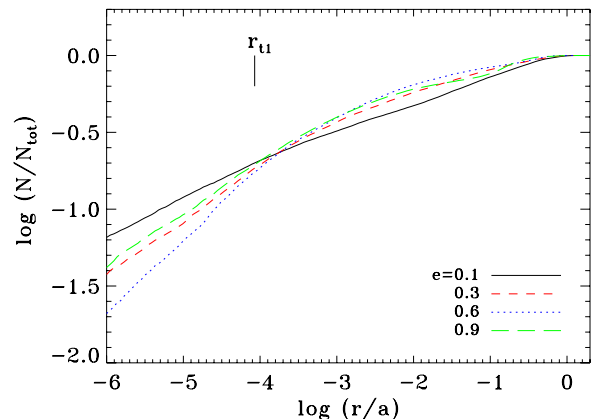


Figure 3. Same as Figure 2, but for $q = 1/81$ and different values of the binary eccentricity e .

(A color version of this figure is available in the online journal.)

vestigate the properties of the disrupted stars. We performed new scattering experiments aimed at covering the whole parameter space of the interacting stellar population, extending the range of semimajor axis a_* from $[a/2, 2a]$ to $[a/20, 20a]$. We ran four sets of numerical experiments, each consisting of 5×10^4 stars, for varying binary eccentricities and $q = 1/81$. A star is counted as disrupted if its separation from the primary hole becomes smaller than r_{t1} . (To calculate r_{t1}/a_0 , the fiducial parameters $M_7 = 1$, $\sigma_{100} = 1$, and $\gamma = 2$ were used.)

5.1. Phase-space Distribution

The semimajor axis of an MBHB typically shrinks by a factor of ~ 10 during the process of cusp erosion via three-body scatterings (Sesana et al. 2008). Below we scale the same scattering experiments and present results for two cases, $a = a_0$ and $a = a_0/10$. Figure 4 shows the distribution of disrupted stars in the $a_*-j_*^2$ plane for $e = 0.1$. The fraction of disrupted stars exceeds 19% in the case $a = a_0/10$ and is close to 13% for $a = a_0$. Many of the stars that get disrupted are initially located outside the tidal loss cone, showing that j_* is not conserved during the three-body interaction; on the other hand, stars initially outside the interaction loss cones get disrupted only rarely. Figure 4 also shows an excess of stars at

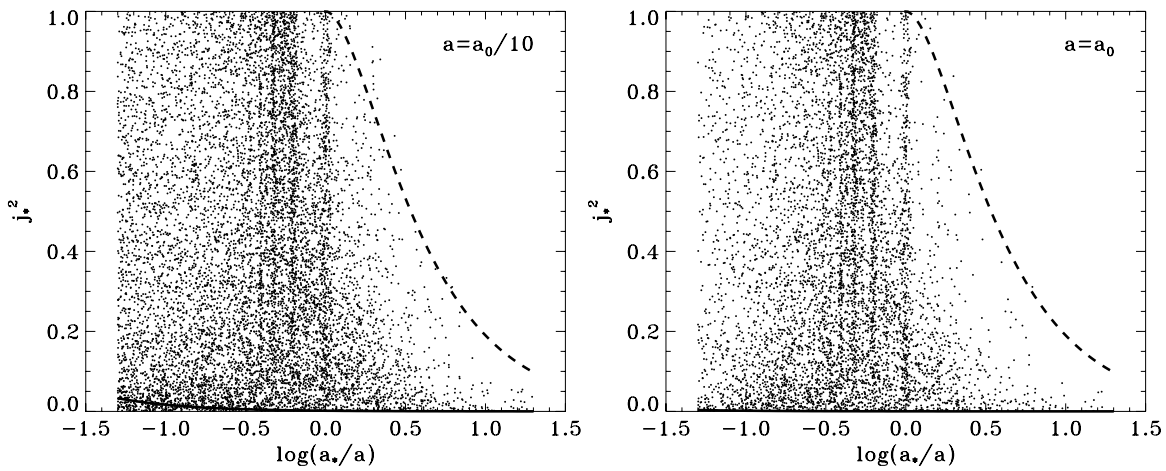


Figure 4. Distribution of disrupted stars in the $a_*-j_*^2$ plane, assuming $e = 0.1$. Left panel: $a = a_0/10$. Right panel: $a = a_0$. The solid and dashed lines delineate, respectively, the tidal loss cones and the interaction loss cones. The parameters of the binary–stellar cusp are $q = 1/81$, $M_7 = 1$, $\sigma_{100} = 1$, and $\gamma = 2$. The excess of disrupted stars at radii $a_* = a(m/n)^{2/3}$, where $m, n = 1, 2, 3, \dots$, is due to resonant interactions.

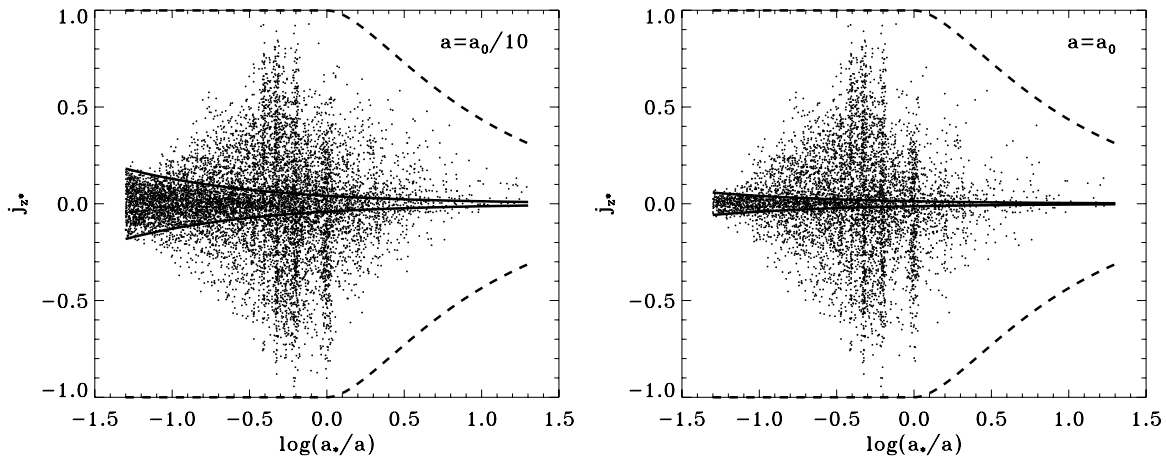


Figure 5. Same as Figure 4 but in the a_*-j_{z*} plane.

the resonance radii $a_* = a(m/n)^{2/3}$, where $m, n = 1, 2, 3, \dots$, indicating the importance of resonant interactions in refilling the tidal loss cone.

For a better understanding of the nature of disrupted stars we depict in Figure 5 their distribution in the a_*-j_{z*} plane. Both theoretical and numerical studies show that for stars that lie inside the binary orbit (with semimajor axis $a_* < a/2$), the angular momentum component parallel to the binary orbital angular momentum, j_{z*} , does not change, while the angular momentum component perpendicular to j_{z*} undergoes secular evolution (Kozai 1962; Lidov 1962). This implies that stars in the wedge-like region $|j_{z*}| < j_{lc}(r_{t1}/a_*)$ will undergo secular evolution and finally enter the tidal loss cone and get disrupted. Figure 5 confirms that the majority of the disrupted stars with $a_* \lesssim a/2$ have $|j_{z*}| \lesssim j_{lc}(r_{t1}/a_*)$, i.e., lie within the region delimited by the solid lines. When $a_* \gtrsim a/2$, however, stars on eccentric orbits cross the orbit of the secondary hole, and can get disrupted even if $|j_{z*}| \gg j_{lc}(r_{t1}/a_*)$. These stars are difficult to model as their orbits are chaotic. The size of the interaction loss cone relative to the Kozai wedge increases with a (r_{t1}/a decreases). As a result, strong chaotic three-body interactions rather than cumulative secular effects are responsible for the majority of the disruptions.

For an isotopic stellar distribution, the fraction of stars having semimajor axis in the range $(a_*, a_* + \Delta a_*)$ that reside inside the

“Kozai wedge” is given by

$$f_K(a_*/a) = \int_{j_{lc}(r_{t1}/a_*)}^{j_{lc}[(1+e)a/a_*]} dj_* \int_{-j_{lc}(r_{t1}/a_*)}^{j_{lc}(r_{t1}/a_*)} dj_{z*} \\ = 2j_{lc}(r_{t1}/a_*)j_{lc}[(1+e)a/a_*] - 2j_{lc}^2(r_{t1}/a_*). \quad (14)$$

In a binary system with $M_7 = 1$, $e = 0.1$, $\sigma_{100} = 1$, $\gamma = 2$, and $a = a_0$, the mean fractions $f_K(a_*/a)$ in the strong-interaction regime $a/2 < a_* < 2a$ are (0.0089, 0.025, 0.044, 0.074) for $q = (1/9, 1/81, 1/243, 1/729)$. These theoretical estimates are significantly smaller than the tidal disruption probabilities derived in Section 4.2 except when $q = 1/9$, highlighting the importance of chaotic interactions in the repopulation of the loss cone. For $q = 1/9$, the theoretical tidal disruption cross section becomes comparable to the numerical one, because stars in the chaotic-interaction regime are more susceptible to early ejection.

Figure 6 shows the distribution of disrupted stars in the a_*-j_{z*} plane for the extreme $e = 0.9$ case. Note that the interaction loss cone is $j_{lc}[(1+e)a/a_*]$ when e is large. The number of disrupted stars increases significantly relative to the low binary eccentricity case, to about 38% when $a = a_0/10$ and 24% when $a = a_0$. This enhancement occurs as more stars now cross the orbit of the secondary hole and interact chaotically

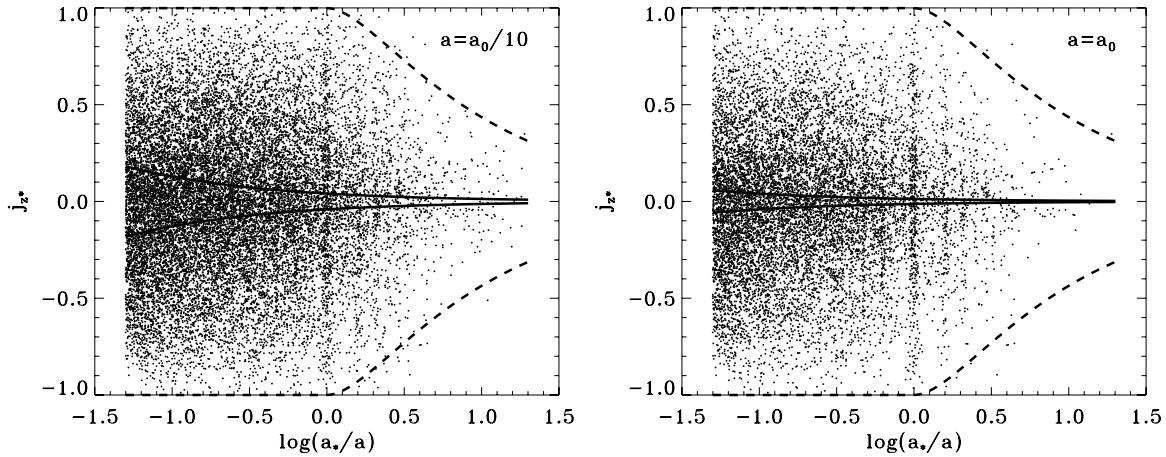


Figure 6. Same as Figure 5 but for $e = 0.9$.

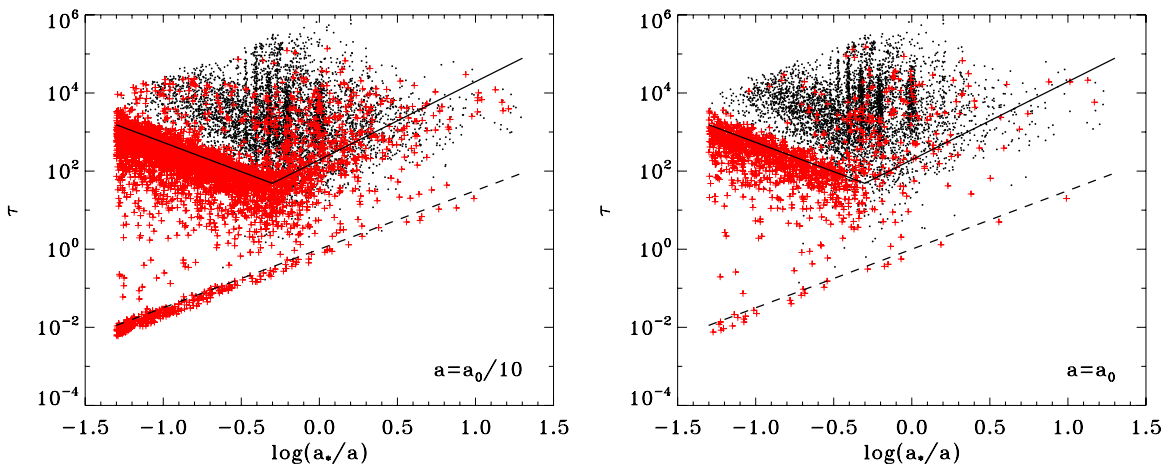


Figure 7. Tidal disruption timescales in unit of the binary period P for $a = a_0/10$ (left panel) and $a = a_0$ (right panel), as a function of the initial semimajor axis of the intruder stars. The dashed line represents the initial stellar orbital periods, and the solid line marks the analytical Kozai timescale given by Equation (19). The red crosses refer to disrupted stars initially inside the Kozai wedge, $|j_{z*}| < j_{lc}(r_{t1}/a_*)$. System parameters as in Figure 4.

(A color version of this figure is available in the online journal.)

with the binary. Moreover, any trace of the Kozai wedge disappears in this case. This is because, when $e = 0.9$, the apoastron of the secondary hole is $0.1a$; therefore, even stars with $a_* \ll a$ experience strong interactions with the secondary hole that destroy the secular, coherent accumulation of the Kozai mechanism.

5.2. Disruption Timescales

During a scattering experiment a bound star may enter the tidal sphere of the primary black hole many times before it is ejected. When calculating the disruption rate, it is the time when the star first crosses r_{t1} that is relevant: in the following, we refer to this time as the “tidal disruption timescale.” In our numerical integrations, we record the times when each star first reaches 21 different separations logarithmically distributed within the range $[\log(100r_{t1}/a_0), \log(r_{t1}/100a_0)]$. Then, for any binary separation between $a_0/100$ and $100a_0$, the tidal disruption timescale can be derived by interpolating between the recorded times. For example, the time when a star reaches $10r_{t1}/a_0$ can be viewed as the tidal disruption timescale (in units of the binary orbital period) when the binary has shrunk to $a = a_0/10$. Figure 7 shows the tidal disruption timescale, τ (in units of the binary period P), as a function of the initial semimajor axis, for $e = 0.1$. The dashed line indicates the stellar orbital period,

$P_* = P(a_*/a)^{3/2}$. The cross symbols clustered around the dashed line represent stars that are disrupted within one orbital period because their initial pericenter distances are smaller than the tidal radius of M_1 . The solid lines in Figure 7 trace instead the Kozai timescale. The formula derived in Equation (10) applies to stars that orbit close to the primary hole while the secondary is far away (“inner problem”). In this case, the quadrupole force exerted by the secondary on the star,

$$F_T \sim (Gm_*M_2a_*)a^{-3}, \quad (15)$$

causes a torque a_*F_T that changes the angular momentum of the star on the timescale

$$T'_K = \frac{J_*}{dJ_*/dt} \simeq \frac{m_*(GM_1a_*)^{1/2}}{a_*F_T} = \frac{P}{2\pi q} \left(\frac{a}{a_*}\right)^{3/2}. \quad (16)$$

In spite of the many simplifications in the derivation of Equation (16), T'_K differs from the actual T_K by only a factor of $4/3$.

Based on our understanding of the Kozai effect in the inner problem, we can now estimate the Kozai timescale for the case of orbit crossing between the intruder star and the secondary hole (“outer problem”). When $a_* \gg a$, the quadrupole force

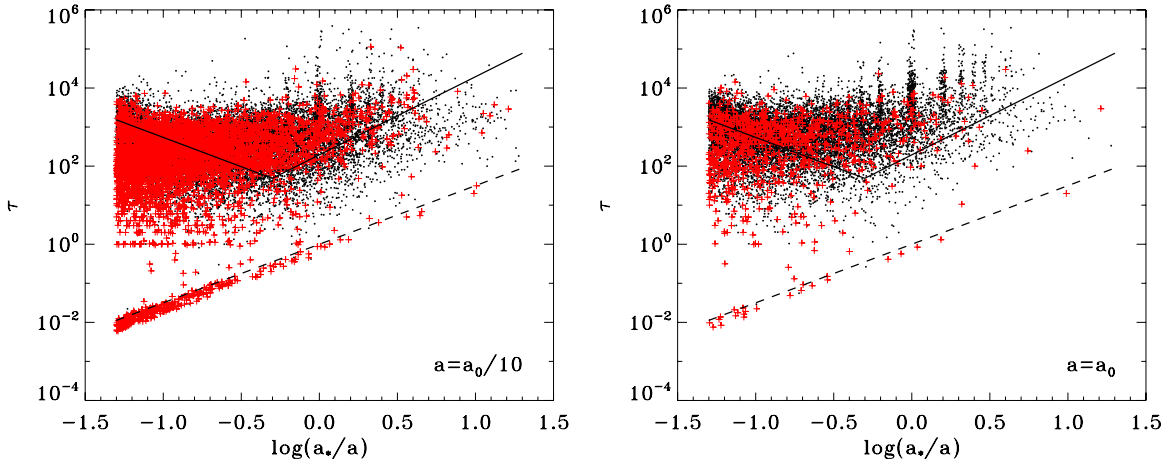


Figure 8. Same as Figure 7 but for $e = 0.9$.

(A color version of this figure is available in the online journal.)

exerted on the star by the binary is

$$F_T \sim \frac{Gm_*M_2a}{a_*^3}, \quad (17)$$

and a_*F_T is the corresponding torque. Since the pericenter of a star must be smaller than a (star lies in the interaction loss cone) for it to be scattered into the tidal loss cone (see Section 5.1), the maximum stellar angular momentum is $m_*j_{lc}(a/a_*)\sqrt{GM_1a_*}$. The Kozai timescale in the outer problem is then given by the ratio of the maximum angular momentum and the torque,

$$T_K \propto \frac{m_*j_{lc}(a/a_*)(GM_1a_*)^{1/2}}{a_*F_T} \propto (a_*/a)^2 P. \quad (18)$$

Since the transition radius between the inner and outer problems is $a_* \sim a/2$, continuity between Equations (10) and (18) yields

$$T_K = \begin{cases} \frac{2}{3\pi q} \left(\frac{a_*}{a}\right)^{-3/2} P & (a_* \leq a/2) \\ \frac{16\sqrt{2}}{3\pi q} \left(\frac{a_*}{a}\right)^2 P & (a_* > a/2) \end{cases}. \quad (19)$$

In Figure 7, the crosses mark stars initially inside the Kozai wedge, so that crosses around the solid lines represent stars fed into the tidal loss cones via the Kozai mechanism. The dots mark instead stars initially outside the Kozai wedge; these participate to the chaotic loss-cone repopulation and are disrupted on timescales that are typically longer than the Kozai timescale. As the binary orbital separation increases, less stars are disrupted by the Kozai mechanism and stars on chaotic orbits make a larger contribution to the repopulation of the tidal loss cones.

Figure 8 shows the tidal disruption timescales for the high eccentricity, $e = 0.9$ case. The cross symbols no longer cluster along the solid lines and the dispersion is larger; this is because resonant interactions are now stronger and partially suppress the secular Kozai evolution.

5.3. Relativistic and Cusp-induced Apsidal Precession

Relativistic effects close to the central MBH and the presence of an extended stellar cusp can both induce the precession of the pericenter of a stellar orbit. These would act to suppress the Kozai mechanism if the associated precession rates were higher than the Kozai rate.

The effect of relativistic precession can be understood as follows. The pericenter of a star with semimajor axis a_* and eccentricity e_* undergoing a secular Kozai evolution processes at an approximate rate

$$\dot{\omega}_K \simeq \frac{5}{(1 - e_*^2)^{1/2}} T_K (a_*)^{-1}. \quad (20)$$

When e_* grows to $e_* \simeq 1 - r_{t1}/a_*$, the star gets tidally disrupted by the primary hole during the pericenter passage. Using $(1 - e_*^2)a_* \simeq 2r_{t1}$ and Equation (19), Equation (20) gives the Kozai precession rate at the tidal disruption radius,

$$\dot{\omega}_K \simeq \begin{cases} \frac{15\pi q}{2\sqrt{2}P(a)} \left(\frac{r_{t1}}{a}\right)^{-1/2} \left(\frac{a_*}{a}\right)^2 & (a_* < a/2) \\ \frac{15\pi q}{32P(a)} \left(\frac{r_{t1}}{a}\right)^{-1/2} \left(\frac{a_*}{a}\right)^{-3/2} & (a_* \geq a/2) \end{cases}. \quad (21)$$

The GR precession rate is instead

$$\dot{\omega}_{GR} \simeq \frac{6\pi GM_1}{(1 - e_*^2)c^2 a_*} P(a_*)^{-1} = \frac{3\pi}{2P(a)} \left(\frac{r_{S1}}{r_{t1}}\right) \left(\frac{a_*}{a}\right)^{-3/2}. \quad (22)$$

The condition $\dot{\omega}_{GR} = \dot{\omega}_K$ admits only one solution, $a_{*,cri} = (8\sqrt{2}\xi)^{-2/7} a$, where

$$\xi \equiv \frac{5q}{16} \left(\frac{r_{t1}}{r_{S1}}\right) \left(\frac{a}{r_{t1}}\right)^{1/2} \quad (23)$$

$$\simeq 1.64 \times 10^3 (3 - \gamma)^{1/2} M_7^{-1/3} \sigma_{100}^{-1} q^{(7-2\gamma)/(6-2\gamma)} \left(\frac{a}{a_0}\right)^{1/2}. \quad (24)$$

If $a_* < a_{*,cri}$, the Kozai evolution is suppressed by GR precession. Note that when $\xi < 1$, $\dot{\omega}_{GR} > \dot{\omega}_K$, and stellar disruptions from the secular Kozai mechanisms are suppressed for the entire stellar population, leaving only chaotic encounters to contribute to the tidal disruption rate in this regime. Since the ratio between the Schwarzschild radius and the tidal radius of an MBH,

$$r_S/r_t \simeq 0.19 M_7^{2/3} (R_\odot/r_*) (M_*/M_\odot)^{1/3}, \quad (25)$$

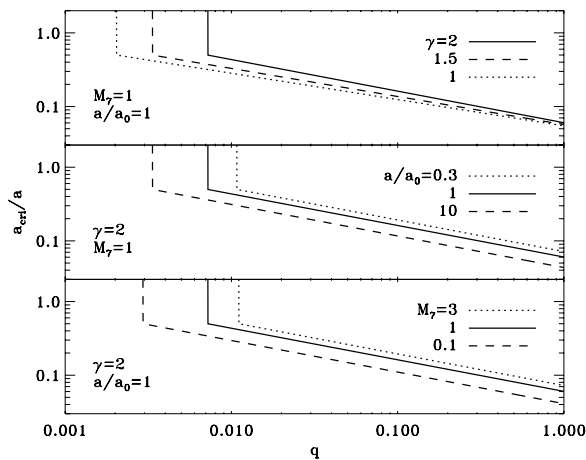


Figure 9. Tracks of $a_{*,\text{cri}}/a$ as a function of q for different values of γ (top), a/a_0 (middle), and M_7 (bottom). The variables are labeled in the top-right corner of each panel, and the fixed parameters in the lower left corner.

increases with hole mass, GR effects typically become important when $M_{\text{BH}} > 3.6 \times 10^6 M_\odot$ (i.e., $r_t < 10r_s$ for solar-type stars).

Figure 9 shows the quantity $a_{*,\text{cri}}/a$ as a function of q for different combinations of the parameters (γ , a/a_0 , M_7), assuming $M_7 \propto \sigma_*^4$ (Tremaine et al. 2002). Following Equations (24) and (9), the curves move toward the upper right direction as r_{t1}/r_{s1} decreases or r_{t1}/a increases. In the upper right corner of each curve in the q - $a_{*,\text{cri}}/a$ plane, the Kozai mechanism is effective, while in the lower left corner $\dot{\omega}_{\text{GR}} > \dot{\omega}_K$ and stellar disruptions are suppressed. When $q \gtrsim 0.01$, the GR precession does not significantly affect the Kozai evolution of stars in the strong-interaction regime ($a_* \in [a/2, 2a]$), when the stellar-disruption fraction is the highest (see Figure 10). For $q \lesssim 0.01$, however, GR effects are important in the strong-interaction regime, especially in the case of steep stellar cusps ($\gamma > 2$), compact MBHBs ($a/a_0 \lesssim 0.3$), or massive primary holes ($M_7 \gtrsim 3$).

To simulate numerically the effects of GR, we have run a series of scattering experiments for different values of q and e using the pseudo-Newtonian potential of Paczyński & Wiita (1980). We integrated the equations of motion

$$\dot{\mathbf{r}} = \mathbf{v} \quad (26)$$

$$\dot{\mathbf{v}} = -G \sum_{i=1}^2 \frac{M_i(\mathbf{r} - \mathbf{r}_i)}{|\mathbf{r} - \mathbf{r}_i|(|\mathbf{r} - \mathbf{r}_i| - r_{Si})^2}, \quad (27)$$

where r_{Si} is the Schwarzschild radius of the i th hole. Each set of experiments followed 10^4 particles sampled in the range $a_* \in [a/20, 20a]$. For illustrative purposes, we calculated r_{Si}/a assuming $a = a_0$, $M_7 = 1$, $\sigma_{100} = 1$, and $\gamma = 2$. For this parameter choice, $r_{t1}/r_{s1} \simeq 5$. The integration of the stellar orbit was stopped at $1.01r_{Si}$ to avoid the singularity at the Schwarzschild radius. Figure 10 compares the fractions of the disrupted particles in the GR versus the non-GR simulations. When $q = 1/9, 1/81$, the suppression of stellar disruptions by relativistic precession is important for $a_* \lesssim a_{*,\text{cri}}$. When $q = 1/243$, $\dot{\omega}_{\text{GR}}$ is always larger than $\dot{\omega}_K$ ($\xi = 0.43$), and tidal disruptions are suppressed over the entire range of a_* .

The impact of an extended stellar cusp on the Kozai evolution can be addressed using similar arguments. The cusp-induced precession rate is (Ivanov et al. 2005; Merritt & Vasiliev 2011)

$$\dot{\omega}_c = K(1 - e^2)^{1/2} \frac{M_*(a_*)}{M_1} \frac{4\pi}{P(a)} \left(\frac{a_*}{a}\right)^{-3/2}, \quad (28)$$

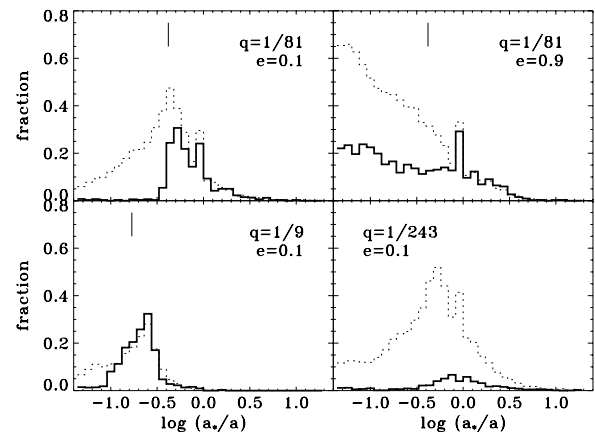


Figure 10. Fraction of disrupted stars in each bin of stellar semimajor axis for the GR (solid histograms) and non-GR (dotted histograms) simulations. The short vertical lines mark the critical radius where $\dot{\omega}_{\text{GR}} = \dot{\omega}_K$. When $q = 1/243$, $\dot{\omega}_{\text{GR}}$ is always larger than $\dot{\omega}_K$.

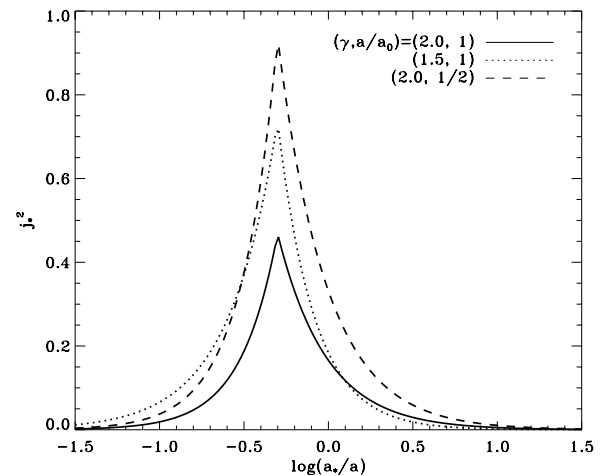


Figure 11. Tracks of $j_{*,\text{cri}}^2$ as functions of a_* for different combinations of the parameters γ and a/a_0 . Stellar orbits satisfying $\dot{\omega}_c < \dot{\omega}_K$ lie below the tracks.

where $K = (0.5, \sqrt{2}/\pi)$ for $\gamma = (2, 1.5)$, respectively, and $M_*(a_*)$ is the stellar mass enclosed within a sphere of radius a_* . The dependence of $\dot{\omega}_c$ on $(1 - e^2)^{1/2}$ indicates that the stellar cusp affects mostly circular orbits. Assuming the broken power-law distribution described in Section 2, the condition $\dot{\omega}_c = \dot{\omega}_K$ corresponds to a critical angular momentum

$$j_{*,\text{cri}}^2 = \begin{cases} (15/16)K^{-1} \left(\frac{a}{a_0}\right)^{\gamma-3} \left(\frac{a_*}{a}\right)^\gamma & (a_* < a/2) \\ (15\sqrt{2}/356)K^{-1} \left(\frac{a}{a_0}\right)^{\gamma-3} \left(\frac{a_*}{a}\right)^{\gamma-7/2} & (a_* \geq a/2) \end{cases}, \quad (29)$$

above which the Kozai effect is suppressed by cusp-induced precession. Figure 11 shows tracks of $j_{*,\text{cri}}^2$ in the a_* - j_*^2 plane: once again, the phase space where the Kozai mechanism can operate is greatly reduced by cusp-induced precession. The suppression is expected to be more significant if a or γ increase, as the stellar mass enclosed by the stellar orbits increases.

We mimicked the effect of a broken power-law stellar cusp (Section 2) by including an external potential in the equations of motion. We set $\gamma = 2$ to maximize the effect of the cusp (see Figure 11), and ran two sets of 10^4 non-GR scattering experiments for $e = 0.1$ and 0.9 , respectively. The binary

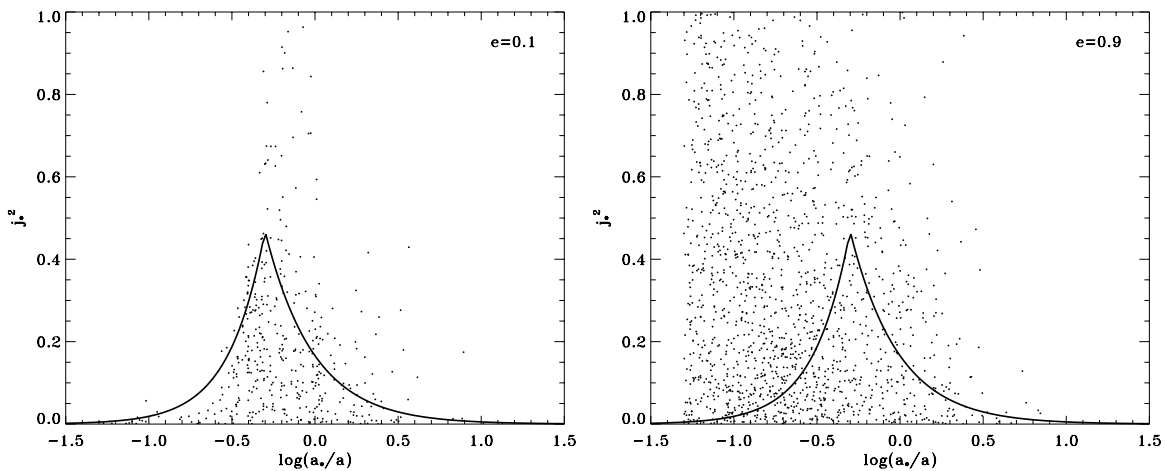


Figure 12. Distribution of disrupted stars in the $a_*-j_*^2$ plane when the potential of a stellar cusp is included (see the text for the parameters of the scattering experiments). The eccentricity of the binary is set to $e = 0.1$ (left) and 0.9 (right). The solid lines show the tracks of $j_{*,cri}^2$.

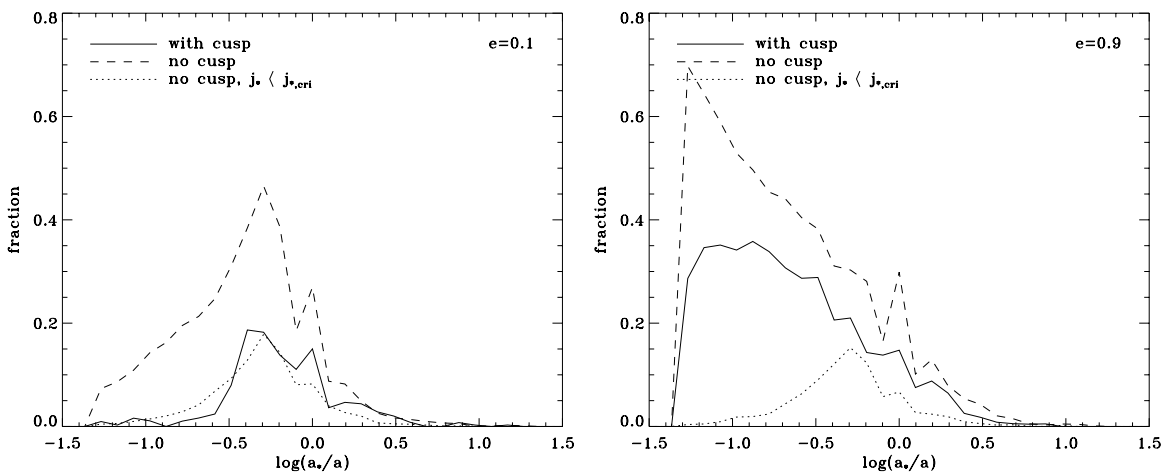


Figure 13. Fraction of disrupted stars as a function of a_* in scattering experiments with (solid curves) and without (dashed curves) the cusp potential. The dotted lines show the disrupted fractions estimated according to the $j_* < j_{*,cri}$ criterion. The left (right) panel assumes $e = 0.1$ ($e = 0.9$).

parameters were set to $q = 1/81$, $e = 0.1$, $M_7 = 1$, $\sigma_{100} = 1$, and $a = a_0$. Figure 12 shows the initial values of a_* , j_*^2 for the disrupted stars, while the fraction of tidal disruptions as a function of a_* is shown in Figure 13. When $e = 0.1$, tidal disruption is almost completely suppressed when $a_* \lesssim a/2$ for stars with $j_* > j_{*,cri}$; when $a_* \gtrsim a/2$ a small fraction of stars with $j_* > j_{*,cri}$ still get disrupted from chaotic interactions. When $e = 0.9$, the suppression of stellar disruptions is also appreciable: a large fraction of stars with $j_* > j_{*,cri}$ are disrupted, however, because their orbits undergo chaotic intersections with the highly eccentric orbit of the secondary MBH. The dotted lines in Figure 13 show that, when e is small, the tidal disruption fraction in the presence of a cusp potential is approximately equal to the fraction of disrupted stars with $j_* < j_{*,cri}$ when the cusp is neglected, with an error that is less than a factor of two. When e is large, however, this method severely underestimates the true disruption fraction because chaotic three-body interactions at $j_* > j_{*,cri}$ are dominant.

6. DISRUPTION RATES FOR STATIONARY BINARIES

Having set the properties of the disrupted stars and tested the limitations of our approximations, we can now proceed to the calculation of the disruption rates. We fix the orbital

separation a and the eccentricity e of the MBHB, and assume that the stellar cusp surrounding M_1 is isotropic and composed of solar-type stars only. The initial stellar distribution function, $f_0(a_*, j_*, j_{z*}) \equiv dn_0/da_*$, can then be written as

$$\frac{dn_0}{da_*} = \frac{2(3-\gamma)}{a_0} \frac{M_2}{M_\odot} \left(\frac{a_*}{a_0}\right)^{2-\gamma}, \quad (30)$$

where dn_0/da_* is the number of stars per unit semimajor axis a_* and the right-hand side follows from the definition of a_0 . We do not consider any sharp cutoff in the stellar distribution caused by stellar collision at small radii. Collisions will likely result in a shallower inner density profile rather than a well-defined cutoff (Freitag & Benz 2002). Moreover, the inner cusp may be repopulated by efficient gas inflow-induced star formation during galaxy mergers (Zier 2006). Here, we assume $\gamma = 2$ and 1.5 to account for this uncertainty.

The stellar disruption rate at time t can then be calculated from

$$\dot{N}_*(t) = \int F(a_*/a, t) (dn_0/da_*) da_*, \quad (31)$$

where $F(a_*/a, t)dt$ is the fraction of stars with semimajor axis a_* that are disrupted in the time interval $(t, t + dt)$. If the loss-cone refilling is entirely due to the Kozai effect, then $F(a_*/a, t)$

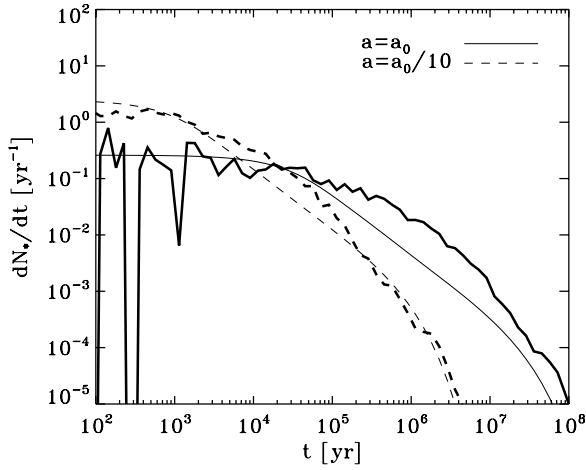


Figure 14. Stellar disruption rates as a function of time for a stationary MBHB with semimajor axis $a = a_0/10$ (solid curves) and $a = a_0$ (dashed curves). The thick lines are the numerical rates derived from scattering experiments, and the thin lines are the analytical rates. System parameters are the same as in Figure 4, and yield $P \simeq (400, 13)$ yr for $a = (a_0, a_0/10)$. Fluctuations in the numerical rates at early times are due to poor statistics.

can be derived analytically as (Ivanov et al. 2005)

$$F(a_*/a, t) = \frac{f_K(a_*/a)}{T_K(a_*/a)} \exp(-t/T_K), \quad (32)$$

where f_K and T_K are given by Equations (14) and (16). The chaotic nature of strong three-body scattering events prevents the possibility of a simple analytical description; therefore, the total disruption rate, including the contribution of resonant interactions, has to be computed numerically from scattering experiments. We divide the $(a_*/20a, 20a_*/a)$ interval into 52 equal logarithmic bins. Given the parameters e and r_{t1}/a , we derive the function $F_i(\tau)$ numerically for each a_*/a bin using the recorded tidal disruption timescales in the corresponding scattering experiments, so that $F_i(\tau)\Delta\tau$ is the fraction of stars in the i th bin that are disrupted in the time interval $(\tau, \tau+\Delta\tau)$. When deriving $F_i(\tau)$, stars sampled in the range $j_*(a_i) < j_c(r_{t1}/a_i)$ are excluded. The total stellar disruption rate at time t is then given by

$$\dot{N}_*(t) = \sum_{i=1}^{52} \frac{F_i(t/P)(dn_0/da_*)(a_i)\Delta a_i}{P}, \quad (33)$$

where a_i and Δa_i are the central semimajor axis and the width of the i th bin. To calculate the numerical stellar disruption rate, one must specify P and dn_0/da_* in physical units. From the definition of a_0 and Equations (11) and (30), we have

$$P \simeq (3 \times 10^5 \text{ yr}) \frac{M_7}{\sigma_{100}^3} Q(3-\gamma)^{3/2} \left(\frac{a}{a_0}\right)^{3/2} \quad (34)$$

with $Q \equiv q^{3/(6-2\gamma)}/(1+q)^{1/2}$ and

$$\frac{dn_0}{da_*} \simeq (4.3 \times 10^6 \text{ pc}^{-1}) q^\alpha \sigma_{100}^2 \left(\frac{a_*}{a_0}\right)^{2-\gamma} \quad (35)$$

with $\alpha \equiv (2-\gamma)/(3-\gamma)$. Figure 14 shows the total stellar disruption rates calculated from Equation (33) for an MBHB with $a = a_0$ and $a = a_0/10$ (and the standard system parameters $q = 1/81$, $e = 0.1$, $M_7 = 1$, $\sigma_{100} = 1$, and $\gamma = 2$).

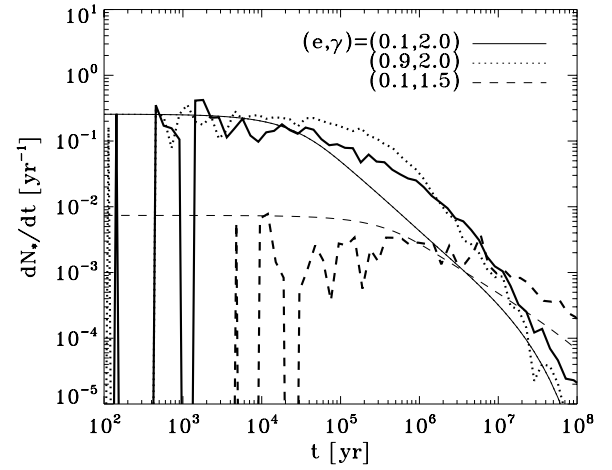


Figure 15. Numerical (thick curves) and analytical (thin curves) stellar disruption rates as a function of time for different combinations of the parameters e and γ (see the text for details). The semimajor axis of the binary is $a = a_0$, and all other system parameters are the same as in Figure 4.

The stellar disruption rate remains constant for a timescale P/q before decreasing rapidly, consistent with the Kozai time scaling. Compared to the rates for single MBHs fed by two-body relaxation, typically 10^{-4} to 10^{-5} yr $^{-1}$, the rates on the plateau are orders of magnitude higher. As a decreases, the plateau rate increases while its duration shortens. Since the Kozai timescale increases as $a^{3/2}$ and the number of stars enclosed in the Kozai wedge scales as $a^{1/2}$, if a shrinks by a factor of 10 the plateau phase becomes a factor of $10^{3/2}$ shorter, while the disruption rate at the plateau increases by a factor of 10. The figure also depicts the analytical disruption rates calculated with Equation (31) for comparison. These agree very well with the numerical results during the plateau phase, indicating that the tidal loss-cone refilling is initially dominated by the Kozai mechanism. At later times, stars inside the Kozai wedge are mostly depleted, and the analytical and numerical rates start to deviate from each other. Deviations in the post-plateau phase increase with increasing binary orbital separations. According to our numerical calculations, about $(1.8 \times 10^4, 1.1 \times 10^5)$ stars with $a/20 < a_* < 20a$ are disrupted over 10^8 years by binaries with $a = (a_0/10, a_0)$. The corresponding numbers in the analytical approximation are $(1.1 \times 10^4, 3.5 \times 10^4)$. The difference highlights the importance of close, resonant encounters with the secondary hole, which change the stellar orbits in a chaotic manner and fuel the tidal loss cone. Figure 15 shows the dependence of the disruption rate on the parameters e and γ . Increasing the binary eccentricity only affects the rate in the post-plateau, chaotic-interaction-dominated phase.

The above results show that, whereas chaotic scatterings dominate the total number of disrupted stars, the Kozai theory provides a reasonably good description of the disruption rate during the plateau phase, as well as the correct order of magnitude of the total number of disruption. We can then use the Kozai theory to predict the scaling of the plateau rate with the system parameters,

$$\dot{N}_* \propto \frac{M_* f_K}{T_K}. \quad (36)$$

Here, M_* is total mass of the interacting stars, $M_* \propto M_1 q (a/a_0)^{3-\gamma}$ (from the definition of a_0), f_K is the fraction of stars in the Kozai wedge, $f_K \propto (r_{t1}/a)^{1/2}$, and T_K is the Kozai timescale, $T_K \propto q^{-1} a^{3/2} M_1^{-1/2}$ (assuming that $a_* \sim a$).

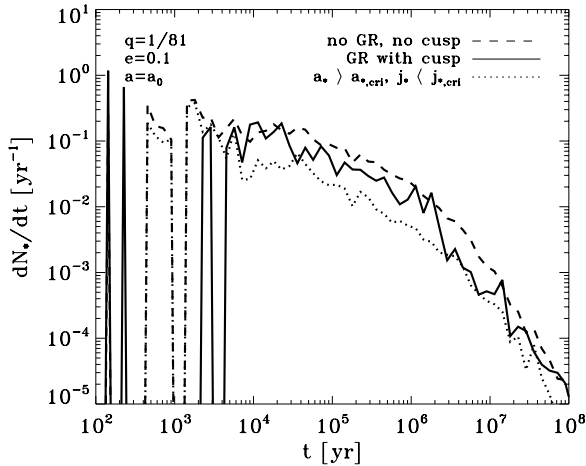


Figure 16. Stellar disruption rates as a function of time for a stationary MBHB with semimajor axis $a = a_0$. Binary parameters are the same as those in Figure 14. The solid line is derived from the scattering experiments where both GR and cusp effects are included, while the dashed line from the experiments when both are neglected. The dotted line is also derived from no-GR/no-cusp experiments, but only using stars with $a_* > a_{*,\text{cri}}$ and $j_* < j_{*,\text{cri}}$.

Substituting into Equation (36), and using the definitions of r_{t1} and a_0 , we finally obtain in the limit $q \ll 1$:

$$\begin{aligned} \dot{N}_* &\propto (3 - \gamma)^{-2} q^{(4-2\gamma)/(3-\gamma)} \left(\frac{a}{a_0}\right)^{1-\gamma} M_1^{-1/3} \sigma_*^4 \\ &\propto (3 - \gamma)^{-2} q^{(4-2\gamma)/(3-\gamma)} \left(\frac{a}{a_0}\right)^{1-\gamma} M_1^{2/3}, \end{aligned} \quad (37)$$

where we have adopted $M_1 \propto \sigma_*^4$ (Tremaine et al. 2002) in the second proportionality. According to Equation (37), when $q = 1/81$, as γ decreases from 2 to 1.5, the peak stellar disruption rate drops by a factor of 40, consistent with the rates in Figure 15. If $\gamma = 2$, the disruption rate is proportional to a^{-1} , consistent with the left panel of Figure 14. The above analysis also implies that, when the stellar density profile is as steep as $\gamma \simeq 2$, the peak stellar disruption rate is not sensitive to q , as shown by Chen et al. (2009). Assuming the M_1 - σ_* relation, the peak rate should be proportional to $M_1^{2/3}$.

To investigate numerically the impact of GR and cusp-induced precession on the stellar disruption rate, we ran an additional set of 10^4 scattering experiments that included the two effects simultaneously (see Section 5.3 for details). The binary parameters were set to $q = 1/81$, $e = 0.1$, $\gamma = 2$, $M_7 = 1$, $\sigma_{100} = 1$, and $a = a_0$. The resulting stellar-disruption rate is shown in Figure 16 with the solid line and is compared to the case in which the two effects are neglected (the dashed line). Because chaotic scatterings are not suppressed by secular effects, the two curves differ by only about a factor of two. The contribution from chaotic scatterings in the GR+cusp experiments can be gauged by the difference between the solid and the dotted curves, the latter derived by considering only stars with $a_* > a_{*,\text{cri}}$ and $j_* < j_{*,\text{cri}}$ in the no-GR/no-cusp experiments. For binaries with larger q , larger e , smaller γ , or larger a/a_0 , stars in the chaotic-interaction regime contribute more to the disrupted stellar fraction, and the GR/cusp-induced suppression of tidal disruptions is milder. Disruptions rates derived by scattering experiments that neglect GR and cusp effects, together with the analytic scalings given by Equation (37), can therefore be considered valid for binaries with $q > 0.01$.

7. DISRUPTION RATES FOR DECAYING BINARIES

Recent calculations based on scattering experiments and ignoring stellar disruptions have suggested that both the binary semimajor axis and eccentricity will evolve rapidly during three-body interactions with ambient bound stars (Sesana et al. 2008). On the one hand, in a shrinking MBHB the interaction loss cone, the tidal disruption timescale, and the cusp stellar distribution all change with time, and this evolution will affect the stellar disruption rate. On the other hand, tidal disruptions halt the exchange of energy and angular momentum between the stars and the binary, altering its dynamical evolution. In order to compute a more realistic tidal consumption rate, a hybrid model is required that takes into account stellar ejections as well as disruptions, and that solves for the time evolution of the binary–stellar cusp system.

In evolving MBHB systems, the ratios r_{S1}/a and $M_*(a)/M_1$ vary with time. In this case, simulating GR and cusp effects becomes extremely time consuming, because additional scattering experiments need to be carried out whenever r_{S1}/a or $M_*(a)/M_1$ changes. For this reason, in this section we do not consider GR and cusp effects, and use the Newtonian scattering experiments without cusp potential to calculate the stellar disruption rate. We restrict the following discussion to the case $q \gtrsim 1/0.01$, where GR and stellar cusp precession suppress the stellar disruption rate by only a factor of two. When $q \ll 0.01$, our test calculations with $q = 1/729$ show that GR and cusp effects can suppress the stellar disruption rate by as much as a factor of 10.

7.1. Fate of Interacting Stars

Figure 17 compares the fraction of stars that are ejected from the system with those that are disrupted in scattering experiments with $q = 1/81$. Tidal disruptions produce two interesting effects: (1) when $a_* \sim a$ a significant fraction of stars experience strong interactions with the secondary hole and cross the tidal radius of M_1 before being ejected; (2) frequent tidal disruptions occur even when $a_* \ll a$, a regime where ejections are rare. These are stars that are driven into the tidal loss cone by the Kozai mechanism. Tidal disruptions have then the double effect of partially suppressing stellar ejections (especially when the binary eccentricity is large) and at the same time of extending inward the influence domain of the binary (the a_*/a interval where the black hole pair can alter the stellar cusp). Figure 18 shows the distributions of changes in specific energy and angular momentum (z -component) for the stars that are ejected and for those that are disrupted. Such distributions are narrowly peaked around zero in the case of the disrupted population, while they are much broader and skewed toward positive values for the ejected component. The evolution of the MBHB is then determined by stellar ejections, since on average the disrupted stars do not exchange energy and orbital angular momentum with the binary.

7.2. Hybrid Model

We finally describe our hybrid model. Given the binary–cusp system parameters q , γ , M_7 , and σ_{100} , we calculate the corresponding value of the initial binary semimajor axis a_0 . We use a_* to describe the absolute semimajor axis of interacting stars, and only consider the relevant portion of the cusp enclosed in the a_* interval $[10^{-3}a_0, 100a_0]$. This range is binned in 100 equally log-spaced bins labeled by the index i , and the initial stellar mass in each bin is given by $m_i = m_* \Delta a_{*,i} dn_0(a_{*,i})/da_*$ ($i = 1, 2, 3, \dots, 100$), where $a_{*,i}$ is the centroid of the i th bin

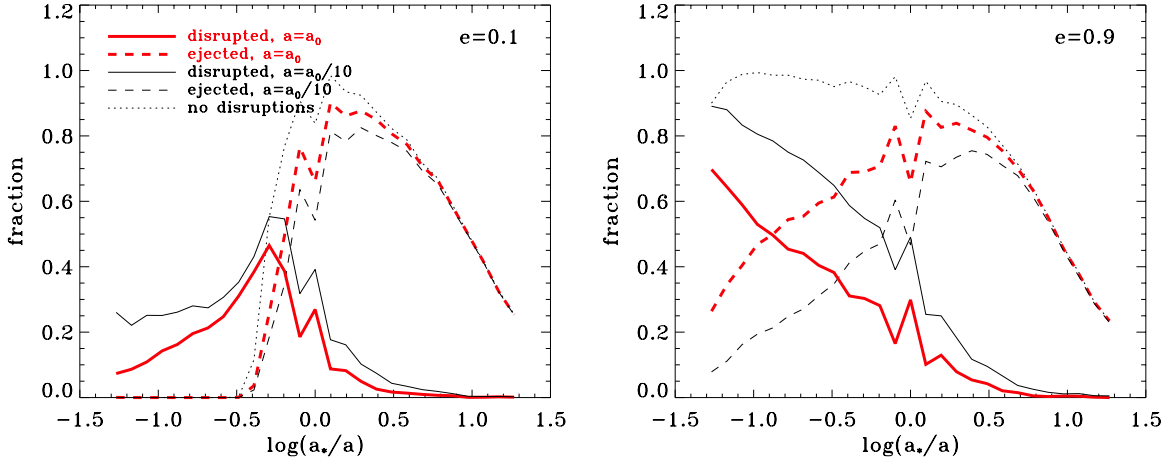


Figure 17. Fractions of disrupted (solid lines) and ejected (dashed lines) stars as a function of stellar semimajor axis a_* for $e = 0.1$ (left panel) and 0.9 (right panel). Black thin lines: $a = a_0/10$. Red thick lines: $a = a_0$. The dotted line shows the ejection fractions if disruptions are not taken into account. All other system parameters are as in Figure 4.

(A color version of this figure is available in the online journal.)

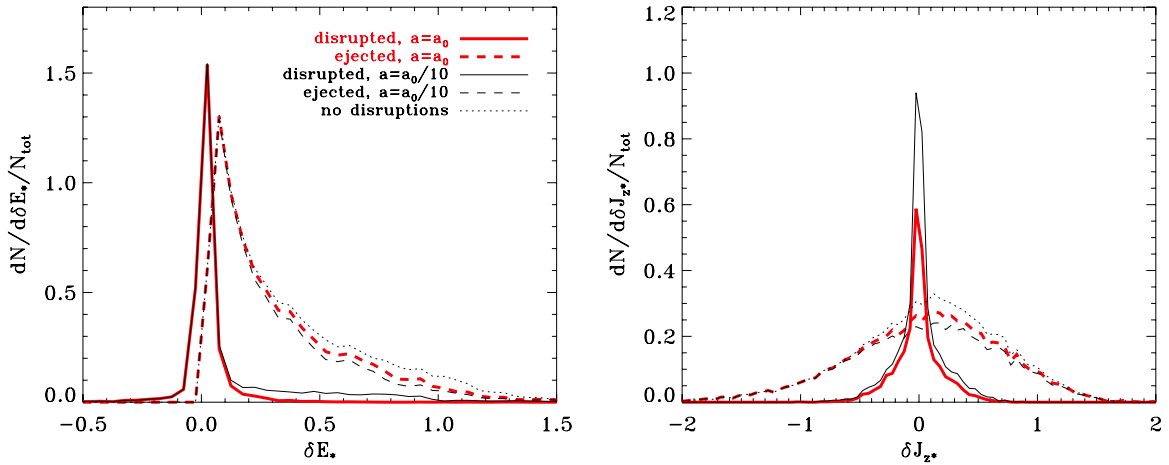


Figure 18. Normalized distributions of changes in specific energy (left panel) and in the z -component of the specific orbital angular momentum (right panel) for the ejected (dashed curve) and disrupted (solid curve) stars when $e = 0.1$. Energy is given in unit of GM_{12}/a , angular momentum in unit of $(GM_{12}a)^{1/2}$. Line styles as in Figure 17.

(A color version of this figure is available in the online journal.)

and $\Delta a_{*,i}$ is the bin width. At $t = 0$ the MBHB is at separation a_0 with eccentricity e_0 and period P_0 ; we then evolve the system numerically forward in time according to the equations

$$a_{k+1} = a_k - \frac{\Delta E_k}{E_k} a_k, \quad (38)$$

$$e_{k+1} = e_k - \frac{1 - e_k^2}{2e_k} \left(\frac{\Delta E_k}{E_k} + \frac{2\Delta J_k}{J_k} \right), \quad (39)$$

where the index k ($k \geq 0$) labels the time step, a_k and e_k are the binary semimajor axis and eccentricity, E_k and J_k are the energy and angular momentum of the binary, and Δ refers to the variation in the k th time step Δt_k . The increments ΔJ_k and ΔE_k depend on the mass $\sum_i \Delta m_{i,k}$ that interacts with the binary in the k th time step. The subtlety lies in properly extracting $\Delta m_{i,k}$ from the set of scattering experiments described in Section 3. Numerical experiments are carried at a fixed binary separation, and the relevant parameter in determining the fate of a star is the ratio $s = a_*/a$. In our runs, we sample the range $1/20 < s < 20$, and this interval is divided in equally log-spaced bins labeled by the index j as s_j . For each s_j bin, we construct the functions

$df/d\tau|_j$, $d\mathcal{E}/d\tau|_j$, and $d\mathcal{J}/d\tau|_j$, which are the differential fractions of ejected stars, mean energy exchange, and mean angular momentum exchange as a function of τ , the time expressed in unit of the binary period. The trick is to assign to each bin $a_{*,i}$ the right s_j value as the binary semimajor axis a evolves, and to properly connect the physical time t describing the evolution of the system to the “scattering experiment time” τ (expressed in units of P). For the time being, let us ignore, for simplicity, the eccentricity evolution. The integration scheme then proceeds as follows.

Consider the first time step Δt_0 . In each $a_{*,i}$ bin, the amount of ejected (or disrupted) mass⁶ in this first time step is

$$\Delta m_{i,0} = m_i \left[\frac{df}{d\tau} \Big|_{j_0} (\tau = 0) \frac{\Delta t_0}{P_0} \right], \quad (40)$$

where j_0 identifies the s_j bin to which the $a_{*,i}$ stellar bin belongs in the first time step. If a particular $a_{*,i}$ bin lies outside the

⁶ Here, we do not distinguish between ejected and disrupted stars. The distribution $df/d\tau$ is actually split into $df/d\tau_{ej}$ and $df/d\tau_{dis}$ to account for both components.

$1/20 < s < 20$ range, then it does not contribute in the evolution of the binary at the considered time step. The binary separation a then evolves according to Equation (38), where

$$\Delta E_0 = \sum_i \left[\frac{d\mathcal{E}}{d\tau} \Big|_{j_0} \left(\tau = 0 \right) \frac{\Delta t_0}{P_0} \right] \Delta m_{i,0} \quad (41)$$

is given by summing over all $a_{*,i}$. We accordingly shrink the binary from a_0 to a_1 .

Consider now the second time step Δt_1 . Since the stellar distribution changes with time, in principle one should carry out new scattering experiments according to the updated stellar distribution to derive $df/d\tau|_j$ at every time step. However, as long as the stars depleted during the previous steps are appropriately excluded, the original scattering experiments can still be used. For the stars in an s_j bin, the elapsed scattering-experiment time $\tau_{j,1}$ during the first time step can be solved from the implicit equation

$$m_i \int_0^{\tau_{j,1}} \frac{df}{d\tau} \Big|_{j_1} d\tau = \Delta m_{i,0}, \quad (42)$$

where $df/d\tau|_j$ is the same function as in the first time step, and j_1 identifies the new s_j bin to which the $a_{*,i}$ stellar bin belongs in the second time step. In the second time step, the time zero point of the function $df/d\tau|_{j_1}$ shifts to $\tau = \tau_{j,1}$ to exclude the stars with depletion timescales shorter than $\tau_{j,1}$, so the interaction mass becomes

$$\Delta m_{i,1} = m_i \left[\frac{df}{d\tau} \Big|_{j_1} \left(\tau = \tau_{j,1} \right) \frac{\Delta t_1}{P_0} \left(\frac{a_1}{a_0} \right)^{-3/2} \right], \quad (43)$$

where $(a_1/a_0)^{-3/2}$ accounts for the change in the period of the binary as it shrinks from a_0 to a_1 . We then evolve again the binary according to Equation (38), where now ΔE_1 is given by

$$\Delta E_1 = \sum_i \left[\frac{d\mathcal{E}}{d\tau} \Big|_{j_1} \left(\tau = \tau_{j,1} \right) \frac{\Delta t_1}{P_0} \left(\frac{a_1}{a_0} \right)^{-3/2} \right] \Delta m_{i,1}. \quad (44)$$

For a generic time step Δt_k , the interacting mass is

$$\Delta m_{i,k} = m_i \left[\frac{df}{d\tau} \Big|_{j_k} \left(\tau = \tau_{j,k} \right) \frac{\Delta t_k}{P_0} \left(\frac{a_k}{a_0} \right)^{-3/2} \right], \quad (45)$$

where j_k identifies the s_j bin to which the $a_{*,i}$ stellar bin belongs in the k th time step, and $\tau_{j,k}$ labels the value of τ that solves the implicit equation:

$$m_i \int_0^{\tau_{j,k}} \frac{df}{d\tau} \Big|_{j_k} d\tau = \sum_{k'=0}^{k-1} \Delta m_{i,k'}. \quad (46)$$

The binary is then evolved according to Equation (38), where ΔE_k is given by replacing the index 1 with k in Equation (44).

In this way, we account for the fact that, in each stellar bin $a_{*,i}$, the interacting fraction in the time step k is governed by the stars left in the bin at that time step following the ejection occurred in the previous time steps and that the ejection occurs at a rate given by the s_{j_k} bin to which the $a_{*,i}$ stellar bin belongs at the k th time step. When we also consider the binary eccentricity evolution, we interpolate the values of $df/d\tau|_j$ and $d\mathcal{E}/d\tau|_j$ between the different eccentricities sampled by the

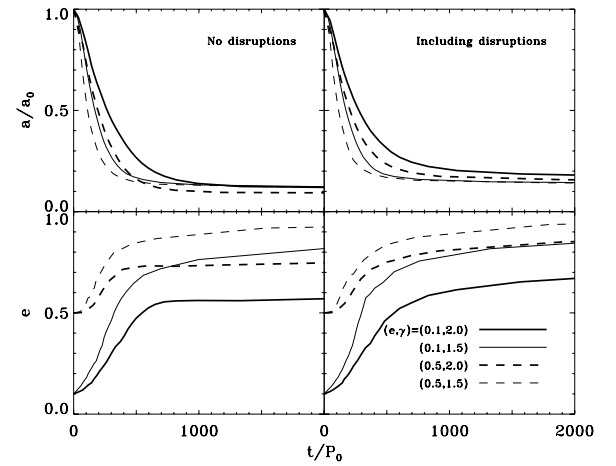


Figure 19. Evolution of binary separation a (top panels) and eccentricity e (bottom panels) for an MBHB with different combinations of the initial e, γ values. The curves in the left panels are computed neglecting tidal disruptions, while those in the right panels include the effect of stellar disruptions. The other system parameters are $q = 1/81$, $M_7 = 1$, and $\sigma_{100} = 1$.

scattering experiments $e = (0.1, 0.3, 0.6, 0.9)$; the eccentricity evolves according to Equation (39), where ΔJ_k is computed from the analogous of Equation (44), but using $d\mathcal{J}/d\tau$. We only considered the variation in the z -component of the angular momentum, because in a spherical stellar cluster the rotational Brownian motion of an MBHB is negligible (Merritt 2002).

Our hybrid approach relies on an adiabatic approximation, i.e., the MBHB orbital evolution is assumed to be slower compared to the typical star–binary interaction timescale. This is certainly true for chaotic encounters, but it is not so for secularly evolving stars. To justify our evolution scheme, we have therefore run test scattering experiments in which the MBHB was evolved by hand, according to the shrinking rates derived with the hybrid model. The initial conditions of the test experiments were the same as in Section 5, and the stellar-disruption rates were calculated following the scheme described in Section 6. This setup allowed us to directly measure the disruption rate caused by an inspiraling binary on a population of stars drawn from a chosen density distribution. Figure 20 compares the stellar-disruption rates derived in this fashion to those given yielded by the hybrid model; the agreement between the two is quite good, validating our orbital integration scheme.

7.3. Results

Figure 19 shows the evolution of an MBHB with $q = 1/81$, $M_7 = 1$, and $\sigma_{100} = 1$ according to our hybrid model. The unit of time, P_0 , is the initial binary orbital period at $a = a_0$, equal to (400, 6700) yr when $\gamma = (2, 1.5)$. When stellar disruptions are not taken into account, the orbital semimajor axis shrinks by a factor of 10 on a timescale of $500P_0$ before the binary stalls: at the same time, the eccentricity increases significantly to $e \simeq 0.5$ – 1 , depending on the initial value and of the parameter γ . When compared with the central panel of Figure 7 in Sesana et al. (2008), the results of the two integration schemes appear to be in excellent agreement. The inclusion of stellar disruptions causes the binary to stall at slightly larger a and higher e . The increase in the stalling radius is caused by the partial suppression of energetic ejections in favor of tidal disruptions. The larger eccentricity increase can be explained as

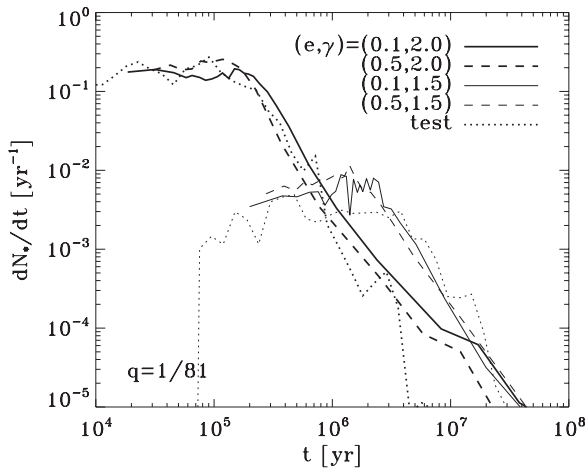


Figure 20. Stellar disruption rates as a function of time for an evolving MBHB with $q = 1/81$, $M_7 = 1$, $\sigma_{100} = 1$, and different combinations of the initial e , γ values of the system. Each dotted curve is derived from 10^4 test scattering experiments in which the MBHB is evolved according to the rates given by the hybrid model (see the solid lines in the right panels of Figure 19). Other line styles as in Figure 19

follows. Sesana et al. (2008) demonstrated that stars with $a_* < a$ tend to drive the binary toward circularization, while stars with $a_* > a$ tend to increase its eccentricity. Since the former are the most susceptible to tidal disruptions, and disrupted stars do not exchange energy and angular momentum with the binary on the average, the relative contribution of stars with $a_* > a$ is larger in the presence of tidal disruptions, pushing the binary eccentricity to higher values. In a realistic situation, the shrinking of the binary would continue at $t > 500P_0$ because of loss-cone diffusion processes and gravitational wave emission, which are not considered in this study.

Figure 20 shows the stellar-disruption rates predicted by the hybrid model (solid and dashed lines) together with those derived by the test scattering experiments with the MBHB evolved by hand (dotted lines). During the first $500P_0$, the rate remains constant, at a level that is comparable to the peak value calculated for a stationary binary. The duration of the plateau, however, is longer in the case of a decaying pair, as new stars are continuously added to the time-varying interaction loss cone. At $t \gtrsim 500P_0$, the evolution time of the MBHB exceeds the tidal disruption timescale, strongly interacting stars get depleted, and the consumption rate drops sharply. The figure also shows that the peak disruption rate is not sensitive to the binary eccentricity but depends on γ according to the scaling relation in Equation (37). After 10^8 yr, the total number of disrupted stars is $(6.5 \times 10^4, 2.3 \times 10^4)$ for $\gamma = (2, 1.5)$. The disruption rate during the plateau phase remains constant even though Equation (37) predicts an increase $\propto a_0/a$ (assuming an isothermal cusp). Equation (37) was derived, however, assuming a stationary binary at different orbital separations in an unperturbed stellar profile. In our hybrid model, the binary shrinks while depleting the stellar cusp, and many of the stars available for disruption at, say, $a = 0.1a_0$ are actually ejected or disrupted during the evolution of the pair from a_0 to $0.1a_0$, leveling off the disruption rate. Given that (1) the disruption rate in the plateau phase remains constant and is consistent with the predictions of the Kozai mechanism even for evolving binaries and (2) the duration of the plateau is of the order of the binary decay timescale, $t_d \propto q^{-3/2}P_0$ (Sesana et al. 2008), the total number of disrupted stars can be scaled according to

$$N_* \propto t_d \dot{N}_* \propto (3 - \gamma)^{-1/2} q^{(2-\gamma)/(6-2\gamma)} M_1^{2/3} \sigma_*^2 \\ \propto (3 - \gamma)^{-1/2} q^{(2-\gamma)/(6-2\gamma)} M_1^{11/12}, \quad (47)$$

where we used Equation (11) for P_0 and the $M_1 - \sigma_*$ relation in the second proportionality. According to the above equation, for $q = 1/81$, N_* should drop by a factor of 2.5 as γ varies from 2 to 1.5, consistent with the numbers derived from our hybrid model. Also, as long as $\gamma \gtrsim 1.5$, N_* should not be very sensitive to the binary mass ratio q . We stress that these scalings are derived from the no-GR/no-cusp experiments, and their validity is limited to binaries with $q > 0.01$.

8. SUMMARY AND CONCLUSIONS

In this paper, we have studied the tidal disruption rate in a system composed by an MBHB and a bound stellar cusp. We have carried out numerical scattering experiments for a detailed investigation of the mechanisms responsible for the repopulation of the tidal loss cone, and developed a hybrid model to self-consistently solve for the evolutions of the binary, the depletion of the stellar cusp, and the stellar consumption rate. Our main results can be summarized as follows.

1. For unequal binaries ($q < 0.1$), the tidal disruption cross section for bound stars, which quantifies the probability of stellar disruption, is three orders of magnitude larger than the cross section for a single MBH fed by two-body relation. Two mechanisms contribute to such enhancement, the Kozai secular effect and chaotic resonant interactions. When the eccentricity of the MBHB is small, stars inside the Kozai wedge repopulate the tidal loss cone on the Kozai timescale, while stars outside the Kozai wedge but inside the interaction loss cone are scattered into the tidal loss cone at random times due to close interactions with the secondary hole. When the eccentricity is large, chaotic loss-cone repopulation becomes dominant over the entire range of stellar semimajor axis $a_* \gtrsim (1 - e)a$.
2. GR and cusp-induced precession quench the Kozai secular evolution of interacting stars, causing a significant suppression (by a factor of ~ 10) of the disruption rate for $q < 0.01$. Therefore, the optimal enhancement of the tidal disruption rate by an MBHB occurs for mass ratios $0.01 < q < 0.1$. Note that even if suppressed by a factor of ~ 10 , the tidal disruption rate for binaries with $q < 0.01$ is still two orders of magnitude larger than that given by standard relaxation processes around a single MBH.
3. If an MBHB with mass ratio $q \ll 1$ does not evolve significantly during $1/q$ revolutions, tidal disruptions of bound stars could initially persist at a constant rate (“plateau phase”) that is 4 dex higher than the typical rates predicted for single MBHs. After one Kozai timescale (evaluated at $a_* = a$), the tidal loss cone is repopulated mainly by chaotic interaction, and the stellar disruption rate decreases with time. The majority of stars are disrupted during a post-plateau later phase.
4. If an MBHB evolves significantly on a timescale of $1/q$ revolution, the plateau phase of stellar disruptions may last longer than a Kozai timescale. Tidal disruptions of bound stars slow down the shrinking of the binary and speed up the growth of binary eccentricity.

Our results indicate that, after the formation of an unequal-mass MBHB at the center of a dense stellar cusp, the tidal

disruption rate may go through three distinct evolutionary phases. The first phase begins shortly after the MBHs become bound and is characterized by a disruption rate as high as 0.1–1 stars per year, resulting from the three-body interactions between the binary and the bound stars (Chen et al. 2009). When the decay timescale of the MBHB becomes longer than the tidal disruption timescales of stars with $a_* \sim a$, a second phase starts, where cusp depletion from slingshot ejections and tidal disruptions causes a sharp drop in the disruption rate. Chen et al. (2008) showed that, unless stellar relaxation is far more efficient than two-body “collisions,” the tidal disruption rate in this phase is orders of magnitudes lower than typical for single MBHs. A third phase begins if the MBHB shrinks to the gravitational wave regime and eventually coalesces. The tidal disruption rate then gradually increases to the value typical for single MBHs, 10^{-5} to 10^{-4} yr^{-1} , within one stellar relaxation timescale (Merritt & Wang 2005). The number of stars disrupted during phase I is about 10^4 – 10^5 for $M_7 = 1$ and $q = 1/81$. The number of stars disrupted in phases II and III depends on the efficiency of stellar relaxation, but would not significantly exceed $\sim 10^5$ – 10^6 . If a galaxy formed, on the average, one unequal-mass MBHB following a minor merger in its lifetime, then the above numbers imply that in a sample of tidal flares from MBHs of $\sim 10^7 M_\odot$, about 10% of events would be associated with binaries. If a galaxy formed unequal-mass MBHBs multiple times during its lifetime, then the detection rate of tidal events from binaries in transient surveys could be higher. Given the very high rates, there is also the possibility to identify MBHBs in galaxies hosting multiple tidal flares within a years-to-decades time span. Over the next decade, synoptic surveys are expected to detect hundreds of tidal disruption candidates. A tidal flare associated with an MBHB is likely interrupted within one orbital period of the binary (Liu et al. 2009), and therefore it is distinguishable from the flares produced by single MBHs, as long as the orbital period of the binary is shorter than the duration of a transient survey. If MBHB-driven disruptions account for 10% of the total rate, then the prospects of identifying MBHBs through tidal flares are promising. Because the predicted rates in the three phases are significantly different from one another, the average stellar disruption rate over the lifetime of a galaxy is sensitive to the infalling rate of secondary MBHs and the relative duration of each phase. A comparison between the observational detection rate of tidal events (Donley et al. 2002; Gezari et al. 2008) and those predicted during the three phases may then shed light on the abundance and dynamical evolution of MBHBs.

Support for this work was provided by NASA through grant NNX08AV68G (P.M.). X.C. and F.K.L. thank the Chinese na-

tional 973 program (2007CB815405), the Research Fund for the Doctoral Program of Higher Education (RFDP), and the China Scholarship Council for financial support. We also acknowledge support from the National Natural Science Foundation of China (11073002). We are grateful to J. Magorrian and F. Haardt for early discussions on this topic. We also thank the referee Hagai Perets whose suggestions really contributed to improve the quality of the manuscript. The scattering experiments were performed on the SGI Altix 330 system at the Astronomy Department, Peking University and the Pleiades cluster at the Department of Astronomy & Astrophysics, University of California, Santa Cruz.

REFERENCES

- Baumgardt, H., Gualandris, A., & Zwart, S. P. 2006, *MNRAS*, **372**, 174
 Begelman, M. C., Blandford, R. D., & Rees, M. J. 1980, *Nature*, **287**, 307
 Chen, X., Liu, F. K., & Magorrian, J. 2008, *ApJ*, **676**, 54
 Chen, X., Madau, P., Sesana, A., & Liu, F. K. 2009, *ApJ*, **697**, L149 (Paper I)
 Colpi, M., & Dotti, M. 2009, *Adv. Sci. Lett.*, in press (arXiv:0906.4339)
 Donley, J. L., Brandt, W. N., Eracleous, M., & Boller, T. 2002, *AJ*, **124**, 1308
 Esquej, P., Saxton, R. D., Freyberg, M. J., Read, A. M., Altieri, B., Sanchez-Portal, M., & Hasinger, G. 2007, *A&A*, **462**, 49
 Freitag, M., & Benz, W. 2002, *A&A*, **394**, 345
 Gezari, S. 2008, *ApJ*, **676**, 944
 Gualandris, A., & Merritt, D. 2009, *ApJ*, **705**, 361
 Hairer, E., Norsett, S. P., & Wanner, G. 1987, *Solving Ordinary Differential Equations I* (1st ed.; Berlin: Springer)
 Innanen, K. A., Zheng, J. Q., Mikkola, S., & Valtonen, M. J. 1997, *AJ*, **11**, 1915
 Ivanov, P. B., Polnarev, A. G., & Saha, P. 2005, *MNRAS*, **358**, 1361
 Kiseleva, L. G., Eggleton, P. P., & Mikkola, S. 1998, *MNRAS*, **300**, 292
 Komossa, S. 2002, *Rev. Mod. Astron.*, **15**, 27
 Kozai, Y. 1962, *AJ*, **67**, 591
 Lidov, M. L. 1962, *Planet. Space Sci.*, **9**, 719
 Lightman, A. P., & Shapiro, S. L. 1977, *ApJ*, **211**, 244
 Liu, F. K., Li, S., & Chen, X. 2009, *ApJ*, **706**, L133
 Matsubayashi, T., Makino, J., & Ebisuzaki, T. 2007, *ApJ*, **656**, 879
 Merritt, D. 2002, *ApJ*, **568**, 998
 Merritt, D., & Milosavljević, M. 2005, *Living Rev. Relativity*, **8**, 8
 Merritt, D., & Poon, M. Y. 2004, *ApJ*, **606**, 788
 Merritt, D., & Vasiliev, E. 2011, *ApJ*, **726**, 61
 Merritt, D., & Wang, J.-X. 2005, *ApJ*, **621**, L101
 Paczyński, B., & Wiita, P. J. 1980, *A&A*, **88**, 23
 Perets, H. B., & Alexander, T. 2008, *ApJ*, **677**, 146
 Perets, H. B., Hopman, C., & Alexander, T. 2007, *ApJ*, **656**, 709
 Quinlan, G. D. 1996, *New Astron.*, **1**, 35
 Rees, M. J. 1988, *Nature*, **333**, 523
 Sesana, A., Haardt, F., & Madau, P. 2006, *ApJ*, **651**, 392
 Sesana, A., Haardt, F., & Madau, P. 2007, *ApJ*, **660**, 546
 Sesana, A., Haardt, F., & Madau, P. 2008, *ApJ*, **686**, 432
 Sesana, A., Haardt, F., Madau, P., & Volonteri, M. 2005, *ApJ*, **623**, 23
 Tremaine, S., et al. 2002, *ApJ*, **574**, 740
 Volonteri, M., Haardt, F., & Madau, P. 2003, *ApJ*, **582**, 559
 Wang, J.-X., & Merritt, D. 2004, *ApJ*, **600**, 149
 Zier, C. 2006, *MNRAS*, **371**, L36